Programming Aggregate States of DNA Nanorods with Sub-10 nm Hydrophobic Patterns for Tunable Cell Entry

Shuting Cao,[†] Lixuan Lin,[†] Yan Zhao, Linjie Guo, Ying Zhu, Lihua Wang, and Jiang Li*

Cite This: *JACS Au* 2023, 3, 1004−1009

Read Online

ACCESS | Metrics & More | Article Recommendations | Supporting Information

ABSTRACT: The intracellular application of DNA nanodevices is challenged by their inadequate cellular entry efficiency, which may be addressed by the development of amphiphilic DNA nanostructures. However, the impact of the spatial distribution of hydrophobicity in cell entry has not been fully explored. Here, we program a spectrum of amphiphilic DNA nanostructures displaying diverse sub-10 nm patterns of cholesterol, which result in distinct aggregate states in the aqueous solution and thus varied cell entry efficiencies. We find that the hydrophobic patterns can lead to discrete aggregate states, from monomers to low-number oligomers ($n = 1−6$). We demonstrate that the monomers or oligomers with moderate hydrophobic density are preferred for cell entry, with up to ∼174-fold improvement relative to unmodified ones. Our study provides a new clue for the rational design of amphiphilic DNA nanostructures for intracellular applications.

KEYWORDS: *DNA nanotechnology, hydrophobic interaction, six-helix bundle, cell uptake, cholesterol, intracellular delivery*
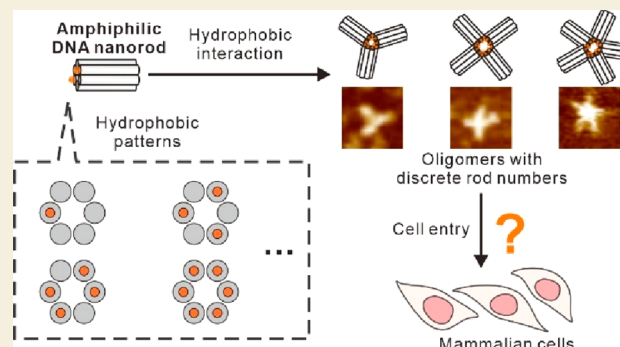
INTRODUCTION

The demonstration of DNA nanostructures in the field of biology and biomedicine has rapidly evolved over the past few decades, showcasing a wide range of possibilities.[1] Given the structural programmability and addressability with nanometer-scale resolution, DNA nanostructures can serve as frameworks to organize various functional moieties such as small molecules, inorganic clusters, and nanoparticles, creating nanoagents, nanodevices, or nanorobots with diagnostic and/or therapeutic functionalities.[2] Particularly, they have been found capable of entering living cells in a size- and shape-dependent manner.[3,4] Compared to many organic/inorganic nanomaterials, DNA nanostructures are intrinsically hydrophilic, anionic, and biodegradable in physiological environments, largely alleviating the concerns about undesired aggregation, cytotoxicity, and cumulative toxicity in living organisms.[4,5] However, compared to conventional amphiphilic nanocarriers (e.g., liposomes and polymeric micelles), plain DNA nanostructures generally show poorer cell entry efficiency, which limits their intracellular applications.[6] There have been several approaches to improving the cellular uptake of DNA nanostructures by coating them with materials such as cationic polymers,[7] peptides,[8] and viral capsid proteins.[9] However, these methods usually compromise the site specificity of DNA nanostructures, and may have the risk of causing cytotoxicity and undesired immune responses.[10]

Recently, a number of rigid amphiphilic DNA nanostructures have been created via decorating hydrophobic moieties on DNA frameworks. These structures have been employed to interact with lipid membranes for a range of applications, such as the construction of synthetic transmembrane receptors, nanopores, and nanochannels,[11−14] the assembly of DNA superstructures on lipid layers,[15−18] the shaping[19−22] and reshaping[23,24] of lipid structures with defined geometries, and the rewiring of intercellular connections.[25,26] On the other hand, amphiphilic DNA nanostructures can form micelle-like aggregates under proper conditions via hydrophobic interactions in aqueous solutions.[27−31] According to several recent studies,[32−34] amphiphilic DNA nanostructures are more effective at entering cells than plain ones, but the correlation between their aggregate states and cell entry efficiency is yet to be explored.

Here, we report the use of DNA nanorods to encode sub-10 nm hydrophobic patterns on their terminals, which could result in various aggregate states in the aqueous solution, including monodispersed rods and micelle-like oligomers with discrete rod numbers (Scheme 1). We found that these different aggregate states in turn led to varied cell entry efficiencies.

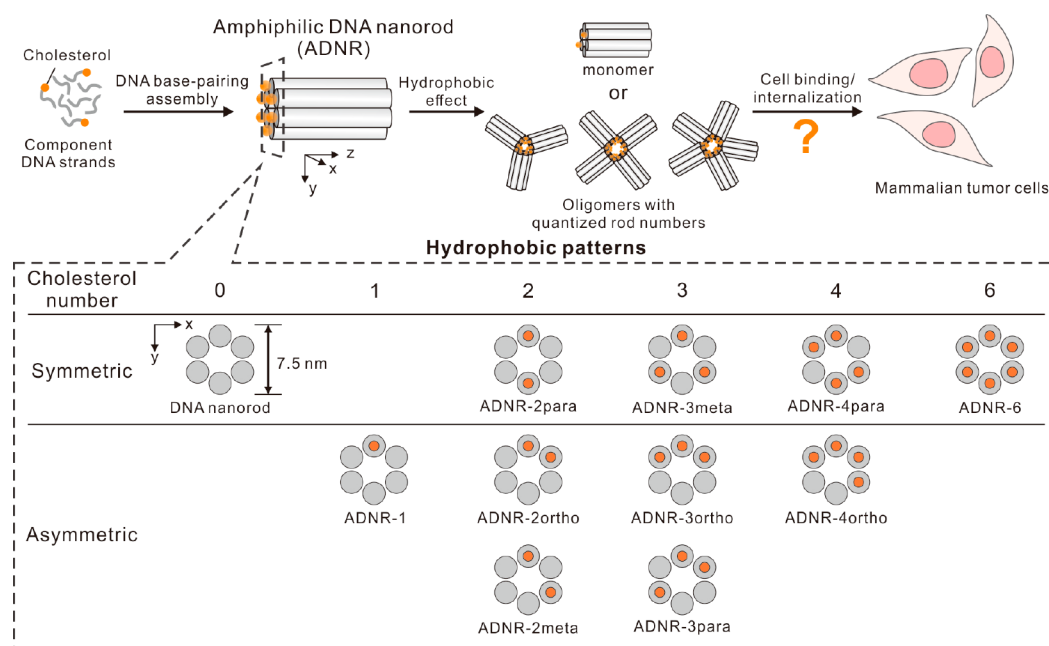**Scheme 1. Concept of Amphiphilic DNA Nanorods (ADNRs) Displaying Programmable Hydrophobic Patterns for Varying Aggregate States and Cell Entry**


RESULTS AND DISCUSSION

First, we designed an amphiphilic DNA nanorod (ADNR) comprising a hydrophilic DNA nanostructure and a cluster of hydrophobic moieties on one side of the former. The DNA nanostructure is adapted from a previously described rod-shaped DNA six-helix bundle with ~22 nm in length and ~7.5 nm in diameter, which is assembled from 20 single-stranded (ss-) DNAs.[33] A given number of cholesterols are located at the ends of certain DNA helices, forming a sub-10 nm-scale hydrophobic pattern displayed on the lateral plane of one terminal (or $x-y$ plane, shown in Scheme 1) of the nanorod. Compared with previously described polyhedral amphiphilic DNA nanostructures,[27,31] this rod-like structure has a long shape (aspect ratio >1), which may resemble the diblock amphiphilic molecules known with cell entry capability.[35] In this way, we designed a spectrum of ADNRs with hydrophobic patterns containing 1−6 cholesterols with different arrangements, termed ADNR-1, ADNR-2ortho, ADNR-2meta, ADNR-2para, ADNR-3ortho, ADNR-3meta, ADNR-3para, ADNR-4ortho, ADNR-4para, and ADNR-6, respectively. Specifically, in ADNR-2para, ADNR-3meta, ADNR-4para, and ADNR-6, the cholesterols were distributed in two-, three-, four- and six-fold rotational symmetry, respectively (referred to as symmetric hydrophobic patterns hereafter); whereas the other structures presented asymmetric hydrophobic patterns. We anticipated that these different hydrophobic patterns may result in various aggregation states of the nanorods in aqueous solutions and consequently vary their cell entry efficiency.

To prepare the ADNRs with the aforementioned hydrophobic patterns, we annealed the component ssDNAs (200 nM each) of the six-helix DNA nanorod structure in the synthesis buffer, with different subsets of them replaced by cholesterol-labeled ssDNAs (detailed in the SI Methods, with the DNA sequences listed in Table S1 and S2). We then characterized the resulting structures with polyacrylamide gel electrophoresis (PAGE) and atomic force microscopy (AFM).

In the gel images (Figure S1), ADNR-1, ADNR-2meta, and ADNR-2para presented a clear band each, with the migration rate approximate to that of the unmodified DNA nanorod (close to the 600-bp marker band), confirming the formation of expected nanorod structures, whereas ADNR-2ortho, ADNR-3ortho, and ADNR-3para presented obvious bands with higher migration rates, indicating the existence of incomplete byproducts. Meanwhile, when the cholesterol number >2, the monomer yield decreased significantly and many of the products were retarded in the gel loading wells, suggesting the formation of aggregates under such conditions. The fractions of aggregates estimated by measuring gel band intensities were ~30.1% (ADNR-3ortho), 28.1% (ADNR-3para) 56.2% (ADNR-3meta), 53.1% (ADNR-4ortho), 60.6% (ADNR-4para), and 53.9% (ANDR-6), respectively, suggesting that their aggregate states varied.

Under AFM (Figure 1a and Figure S2), we observed that ADNR-1, ADNR-2para, and ADNR-2meta appeared mostly as monodispersed rod-like particles, with a height similar to that of the unmodified DNA nanorods. ADNR-2ortho formed particle-like structures with a lower height, suggesting that the structures were not intact six-helix nanorods, in agreement with the gel electrophoresis. ADNR-3para and ADNR-3ortho were mostly monomers, with some irregular aggregates (Figure S2). Interestingly, ADNR-3meta, ADNR-4ortho, ADNR-4para, and ADNR-6 formed many flower-like oligomers with ~3 (2−3, with 3 the highest frequency), 4 (2−5), 4 (2−5) and 5 (3−6) branches, respectively (shown in Figure 1b, c and Figure S2), which should be the head-to-head aggregates of the ADNRs driven by hydrophobic interaction. Their branches could be unambiguously resolved by AFM, allowing us to count the rod number per oligomer.

Based on the above observation, we found that the arrangement of cholesterols could affect the formation of the six-helix nanorods and their aggregate states. In general, symmetric cholesterol patterns (e.g., ADNR-2para, and ADNR-3meta) showed higher yields of monomers or flower-
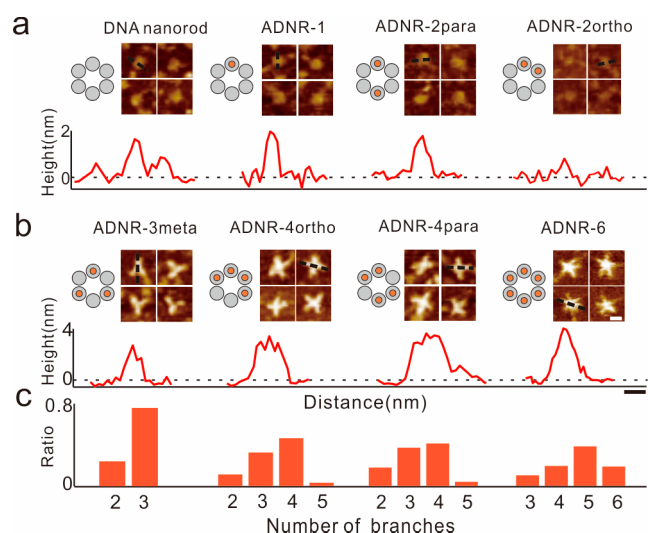
Figure 1. AFM of ADNRs series structures. (a, b) Representative AFM images of ADNRs in the states of (a) monomers and (b) flower-like oligomers, with corresponding line profiles across the structures (marked with blank dashes). Scale bar, 20 nm. (c) Frequency distributions of the branch numbers of the flower-like oligomers in b.

like oligomers compared to asymmetric ones with equivalent cholesterol numbers (ADNR-2ortho, ADNR-2meta, ADNR-3ortho, and ADNR-3para), particularly when the cholesterol number was 2−3. The reduced yields of well-organized structures resulting from asymmetric cholesterol patterns may be due to the unevenly high local hydrophobicity, which could interfere with DNA self-assembly in aqueous solutions.

On the other hand, we could conclude that the rod number per oligomer is generally positively correlated with the cholesterol number in each ADNR, which could be attributed to the hydrophobicity increasing with the cholesterol number. When the cholesterol number per ADNR was <3, the concentration of ADNRs in our study was below their critical micelle concentration (CMC), thus mostly presenting as monomers; whereas when the cholesterol number was >3, flower-like oligomers formed. Interestingly, oligomers with a rod number >6 were rare in our observation, suggesting that the scale of amphiphilic assembly might be self-limited due to the strong steric hindrance arising from the rigid DNA frameworks. Collectively, by programming the sub-10 nm hydrophobic patterns of ADNR, we could obtain different aggregates states with discrete rod numbers (1−6) in the aqueous solution.

To investigate the cell entry of the ADNRs with different aggregate states, we incubated Alexa488-labeled ADNRs (100 nM each) with MCF-7 cells (1640 medium, 0.5% serum, 37 °C, 5% CO_2) for cytometric analysis. Here, we chose ADNR-1, ADNR-2para, ADNR-3meta, ADNR-4para, and ADNR-6 for comparison, which could effectively yield structures in the aqueous solution with rode numbers of ~1, 1, 3, 4, and 5, respectively. In this experiment, the molar concentration of the ADNR monomers was held constant at 100 nM. First, we analyzed the ensemble results measured by flow cytometry (Figure 2). We found that all the ADNRs exhibited much higher cell binding than unmodified DNA nanorods. After 8 h of cell incubation, ADNR-1, ADNR-2para, ADNR-3meta, ADNR-4 para, and ADNR-6 resulted in ~34-, 174-, 122-, 99-, and 20-fold increases in cellular fluorescence intensity,
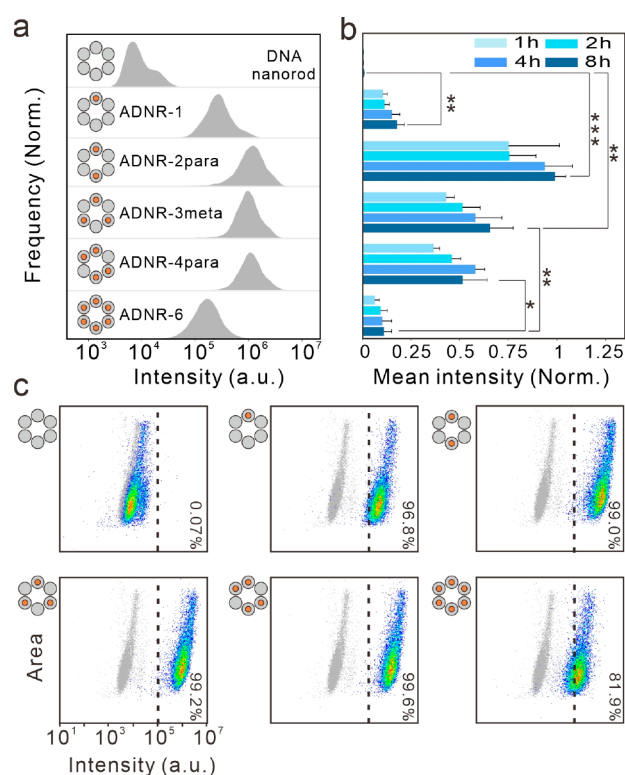
Figure 2. Effect of the cholesterol pattern on cell binding efficiency. (a) Representative cytometric fluorescence intensity distributions indicating cell binding of different ADNRs at 8 h. (b) Mean fluorescence intensities (normalized to the highest fluorescence in each replicate) of the cytometric results at 1, 2, 4, and 8 h, respectively. Error bars, SD of three independent tests. * $p < 0.05$, ** $p < 0.005$, *** $p < 0.0001$, determined by one-way ANOVA comparison. (c) Representative scatter plots of cell fluorescence distributions after being treated with the structures for 8 h. Gray spots, blank cells.

respectively, relative to the unmodified DNA nanorods (Figure 2a, b). In addition, the percentages of fluorescently positive cells (fluorescence intensity >10^5 a.u.) at 8 h were ~0.07% (unmodified DNA nanorods), 96.8% (ADNR-1), 99% (ADNR-2para), 99.2% (ADNR-3meta), 99.6% (ADNR-4para), and 81.9% (ADNR-6), respectively (Figure 2c), suggesting that the vast majority of the cells could bind to these ADNRs. Collectively, these results confirmed that amphiphilic DNA structures are overall favored in cell binding and entry, in agreement with previous studies.[32,33,36,37] Notably, ADNR-2para and ADNR-3meta (mostly formed monomers and three-branch oligomers) led to higher cell fluorescence than others, suggesting that the cell binding efficiency was not unidirectionally increasing with the rod number.

To gain a deeper understanding of the cell entry process of these structures, we employed confocal imaging to inspect individual cells that were treated with the representative ADNRs (Figure 3a and Figure S3). The results showed that at 1 h, intense fluorescence of ADNR-2para and ADNR-3meta appeared on the cell membranes and partially outlined the cells, whereas the fluorescence signals from other structures were weak. At 4 h, the membrane fluorescence signals of ADNR-2para and ADNR-3meta were further enhanced; some signals of ADNR-2para appeared inside the cell; while intense signals of ADNR-4para appeared both on the cell membranes
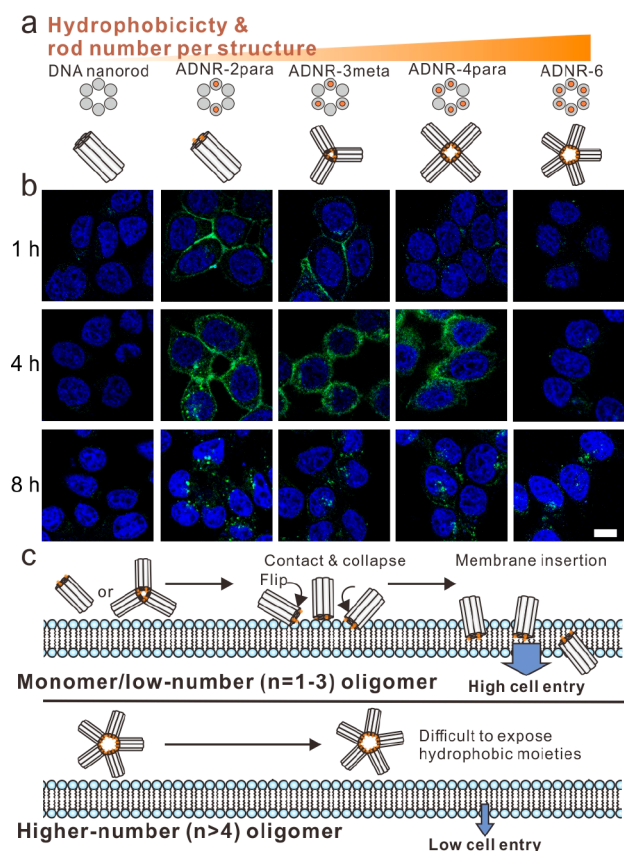
Figure 3. Cell entry of ADNRs with different aggregate states. (a) Confocal images of MCF-7 cells incubated with ADNRs for 1, 4, and 8 h, respectively. Blue, nucleus stained by Hoechst 33258. Green, ADNRs labeled with Alexa 488. Scale bar, 10 μm. (b) Cartoon of the presumed mechanism underlying the difference in cell entry efficiency.

and in the cells. At 8 h, the fluorescence speckles were mostly located inside the cells; meantime, sparse fluorescence speckles of ADNR-6 also appeared inside the cells. During the whole observation, the cellular fluorescence of unmodified nanorods remained minimal. These results revealed the processes of the cell entry of these structures. In general, ADNR-2para and ADNR-3meta could more rapidly and efficiently enter the cells than other structures; the further increase of cholesterol number and rod number (ADNR-4para and ADNR-6) led to decreased cell entry kinetics. These results were consistent with the flow cytometric measurements. In addition, we can conclude that after 8 h incubation, these structures were mostly located inside the cells. Hence, the fluorescence intensities obtained by flow cytometry at 8 h could quantitatively reflect their cell entry efficiency. In addition, we evaluated the cytotoxicity of the ADNRs using CCK8 assay. The results showed that even with much enhanced cell entry efficiencies (including ADNR-2para and ADNR-3meta), these structures at the dosage used in this study (100 nM) showed no suppression to cell viability after 24 h of cell incubation, suggesting minimal cytotoxicity of these structures (Figure S4).

These results together suggest that the hydrophobic pattern displayed on ADNR plays an important role in its cell entry. Although hydrophobicity in general benefits cell entry, their correlation is not unidirectional. The monomers or low-number oligomers with modest hydrophobicity (2 or 3 cholesterols) show high cell entry efficiencies (∼2 orders of

magnitude than the unmodified structure). We reason that the modest hydrophobicity allows the monomers/oligomers to flip and expose the hydrophobic groups to cell lipid membranes easily, leading to effective cell binding and entry (Figure 3b). On the contrary, an overhigh hydrophobicity (e.g., 6 cholesterols) might lead to more stable micelle-like structures, which are difficult to collapse and expose the buried hydrophobic moieties to the cell membrane, leading to decreased cell entry efficiency.

CONCLUSIONS

In summary, we in this study demonstrated the programming of sub-10 nm hydrophobic patterns on DNA nanorods, which enabled the modulation of their aggregation state and consequently their cell binding efficiencies. We conclude that DNA nanostructures carrying modestly hydrophobic groups (rather than highly hydrophobic ones) may show optimal cell entry efficiency (∼2 orders of magnitude improvement), which could be due to the restricted aggregation with high accessibility of hydrophobic groups to cell membranes.

This system also shows two advantages. First, the six-helix DNA nanorod possesses addressability with ∼2 nm resolution (i.e., the diameter of a DNA double-helix) on its end, allowing high-density patterning of hydrophobic moieties at the sub-10 nm scale. Compared to wide-space distributions (e.g., placed on different sides of a polyhedron[14]), the focused distribution of hydrophobic moieties at one end might contribute to the high cell entry efficiency (2 orders of magnitude improvement) in a "point attack" manner, as suggested in previous studies.[38] Second, the shape and rigidity of the DNA nanorods allow for the formation of flower-like oligomers with discrete numbers of branches, enabling quantifiable analysis with AFM. This led to conclusions that would be difficult to obtain with conventional DNA micelles composed of indeterminate numbers of single-stranded or double-stranded DNAs.[39] In future work, we would endeavor to reveal the specific cell entry pathways of these amphiphilic structures and the underlying mechanisms.[34,40] The possibility of lysosomal escaping and the potential of them for cytosol delivery of theranostic agents would also be investigated.[41] Overall, our study may provide a new clue for the rational design of effective nanocarriers based on amphiphilic DNA nanostructures for intracellular applications.

METHODS

Preparation of ADNRs

DNA nanorods were fabricated using a simple one-pot process. Specifically, 20 strands (6HB-1−6HB-20 listed in Table S1) were mixed thoroughly at equal concentrations of 200 nM in 500 μL of synthetic buffer (composed of 40 mM Tris, 20 mM acetic acid, 2 mM EDTA, and 12.5 mM magnesium acetate, pH 8.0), and then slowly cooled from 90 °C to room temperature in a water bath within a 1 L styrofoam box. To fabricate ADNRs with different hydrophobic patterns, some of the sequences were replaced by cholesterol-modified ones (detailed in Table S2), with all other conditions unchanged.

AFM Imaging

For AFM imaging, 8 μL of the DNA structure sample (100 nM) in the synthetic buffer was spotted on the mica surface (pretreated by 3-aminopropyltriethoxysilane, or APTES, for 1.5 min before washing by Milli-Q water), and was allowed to absorb onto the surface for 5 min. Then, the sample was

scanned on a Bruker atomic force microscope using fluid+ (Veeco Inc., USA) tips.

Analysis of Cellular Uptake of ADNRs

The MCF-7 cells were cultured in 1640 medium (Invitrogen) under humidified air with 5% CO_2 at 37 °C. Prior to use, the cells were seeded overnight in 12-well culture plates at a density of 1.5×10^5 cells/well. Upon reaching ~70% cell density, the cells were exposed to ADNRs for 1, 2, 4, or 8 h in 1640 medium supplemented with 0.5% (v/v) FBS at 37 °C. Flow cytometry (Beckman, USA) was utilized to determine the fluorescence intensity of the cells after incubation. Three replicates were performed for each group, with ~10^4 cells collected per replicate. For confocal imaging, the cells were seeded on 35 mm glass bottom dishes at a density of ~7×10^4 cells/well and were cultured and treated with ADNRs under the same conditions as above. The cells were then stained with Hoechst for nuclei and washed with PBS three times. A laser confocal microscope (Zeiss LSM980) was used to obtain images, with wavelength sets of 405 nm Ex/415−480 nm for Hoechst and 488 nm Ex/500−540 nm for Alexa488.

■ ASSOCIATED CONTENT

Ⓢ Supporting Information

The Supporting Information is available free of charge at https://pubs.acs.org/doi/10.1021/jacsau.3c00097.

Supplementary experimental details, polyacrylamide gel electrophoresis images, wide-view AFM images, confocal images, and tables of DNA sequences (PDF)

■ AUTHOR INFORMATION

Corresponding Author

Jiang Li − *Division of Physical Biology, CAS Key Laboratory of Interfacial Physics and Technology, Shanghai Institute of Applied Physics, Chinese Academy of Sciences, Shanghai 201800, China; University of Chinese Academy of Sciences, Beijing 100049, China; The Interdisciplinary Research Center, Shanghai Synchrotron Radiation Facility, Shanghai Advanced Research Institute, Chinese Academy of Sciences, Shanghai 201210, China; Institute of Materials Biology, Shanghai University, Shanghai 200444, China;* ⓞ orcid.org/0000-0003-2372-6624; Email: lijiang@sinap.ac.cn

Authors

Shuting Cao − *Division of Physical Biology, CAS Key Laboratory of Interfacial Physics and Technology, Shanghai Institute of Applied Physics, Chinese Academy of Sciences, Shanghai 201800, China; University of Chinese Academy of Sciences, Beijing 100049, China; The Interdisciplinary Research Center, Shanghai Synchrotron Radiation Facility, Shanghai Advanced Research Institute, Chinese Academy of Sciences, Shanghai 201210, China*

Lixuan Lin − *Division of Physical Biology, CAS Key Laboratory of Interfacial Physics and Technology, Shanghai Institute of Applied Physics, Chinese Academy of Sciences, Shanghai 201800, China; University of Chinese Academy of Sciences, Beijing 100049, China; The Interdisciplinary Research Center, Shanghai Synchrotron Radiation Facility, Shanghai Advanced Research Institute, Chinese Academy of Sciences, Shanghai 201210, China*

Yan Zhao − *Institute of Biomedical Health Technology and Engineering, Shenzhen Bay Laboratory, Shenzhen 518132, China*

Linjie Guo − *The Interdisciplinary Research Center, Shanghai Synchrotron Radiation Facility, Shanghai Advanced Research Institute, Chinese Academy of Sciences, Shanghai 201210, China; Institute of Materials Biology, Shanghai University, Shanghai 200444, China*

Ying Zhu − *Division of Physical Biology, CAS Key Laboratory of Interfacial Physics and Technology, Shanghai Institute of Applied Physics, Chinese Academy of Sciences, Shanghai 201800, China; University of Chinese Academy of Sciences, Beijing 100049, China; The Interdisciplinary Research Center, Shanghai Synchrotron Radiation Facility, Shanghai Advanced Research Institute, Chinese Academy of Sciences, Shanghai 201210, China; Institute of Materials Biology, Shanghai University, Shanghai 200444, China*

Lihua Wang − *Division of Physical Biology, CAS Key Laboratory of Interfacial Physics and Technology, Shanghai Institute of Applied Physics, Chinese Academy of Sciences, Shanghai 201800, China; University of Chinese Academy of Sciences, Beijing 100049, China; The Interdisciplinary Research Center, Shanghai Synchrotron Radiation Facility, Shanghai Advanced Research Institute, Chinese Academy of Sciences, Shanghai 201210, China; Institute of Materials Biology, Shanghai University, Shanghai 200444, China*

Complete contact information is available at:
https://pubs.acs.org/10.1021/jacsau.3c00097

Author Contributions

[†]S.C. and L.L. contributed equally. CRediT: **Shuting Cao** data curation, formal analysis, investigation, methodology, visualization, writing-original draft; **Lixuan Lin** data curation, formal analysis, investigation, methodology, visualization; **Yan Zhao** conceptualization, methodology, resources; **Linjie Guo** conceptualization, investigation, supervision, validation; **Ying Zhu** resources, supervision; **Lihua Wang** project administration, resources; **Jiang Li** conceptualization, funding acquisition, project administration, supervision, writing-review & editing.

Notes

The authors declare no competing financial interest.

■ ACKNOWLEDGMENTS

■ REFERENCES

(1) Jiang, S. X.; Ge, Z. L.; Mou, S.; Yan, H.; Fan, C. H. *Chem.* **2021**, 7, 1156−1179.

(2) Seeman, N. C.; Sleiman, H. F. *Nat. Rev. Mater.* **2018**, 3, 17068.

(3) Alemdaroglu, F. E.; Alemdaroglu, N. C.; Langguth, P.; Herrmann, A. *Macromol. Rapid Commun.* **2008**, 29, 326−329.

(4) Bastings, M. M. C.; Anastassacos, F. M.; Ponnuswamy, N.; Leifer, F. G.; Cuneo, G.; Lin, C.; Ingber, D. E.; Ryu, J. H.; Shih, W. M. *Nano Lett.* **2018**, 18, 3557−3564.

(5) Wang, P.; Rahman, M. A.; Zhao, Z.; Weiss, K.; Zhang, C.; Chen, Z.; Hurwitz, S. J.; Chen, Z. G.; Shin, D. M.; Ke, Y. *J. Am. Chem. Soc.* **2018**, 140, 2478−2484.

(6) Jin, J.-O.; Park, H.; Zhang, W.; de Vries, J. W.; Gruszka, A.; Lee, M. W.; Ahn, D.-R.; Herrmann, A.; Kwak, M. *Biomaterials* **2017**, 115, 81−89.

(7) Sun, W.; Ji, W.; Hall, J. M.; Hu, Q.; Wang, C.; Beisel, C. L.; Gu, Z. *Angew. Chem., Int. Ed.* **2015**, *54*, 12029−12033.

(8) Ponnuswamy, N.; Bastings, M. M. C.; Nathwani, B.; Ryu, J. H.; Chou, L. Y. T.; Vinther, M.; Li, W. A.; Anastassacos, F. M.; Mooney, D. J.; Shih, W. M. *Nat. Commun.* **2017**, *8*, 15654.

(9) Mikkila, J.; Eskelinen, A. P.; Niemela, E. H.; Linko, V.; Frilander, M. J.; Torma, P.; Kostiainen, M. A. *Nano Lett.* **2014**, *14*, 2196−2200.

(10) Hu, Q.; Wang, S.; Wang, L.; Gu, H.; Fan, C. *Adv. Healthc. Mater.* **2018**, *7*, 1701153.

(11) Diederichs, T.; Pugh, G.; Dorey, A.; Xing, Y. Z.; Burns, J. R.; Hung Nguyen, Q.; Tornow, M.; Tampe, R.; Howorka, S. *Nat. Commun.* **2019**, *10*, 5018.

(12) Thomsen, R. P.; Malle, M. G.; Okholm, A. H.; Krishnan, S.; Bohr, S. S. R.; Sorensen, R. S.; Ries, O.; Vogel, S.; Simmel, F. C.; Hatzakis, N. S.; Kjems, J. *Nat. Commun.* **2019**, *10*, 5655.

(13) Maingi, V.; Burns, J. R.; Uusitalo, J. J.; Howorka, S.; Marrink, S. J.; Sansom, M. S. P. *Nat. Commun.* **2017**, *8*, 14784.

(14) Chidchob, P.; Offenbartl-Stiegert, D.; McCarthy, D.; Luo, X.; Li, J.; Howorka, S.; Sleiman, H. F. *J. Am. Chem. Soc.* **2019**, *141*, 1100−1108.

(15) Avakyan, N.; Conway, J. W.; Sleiman, H. F. *J. Am. Chem. Soc.* **2017**, *139*, 12027−12034.

(16) Kocabey, S.; Kempter, S.; List, J.; Xing, Y.; Bae, W.; Schiffels, D.; Shih, W. M.; Simmel, F. C.; Liedl, T. *ACS Nano* **2015**, *9*, 3530−3539.

(17) Zhang, Y.; He, X.; Zhuo, R.; Sha, R.; Brujic, J.; Seeman, N. C.; Chaikin, P. M. *Proc. Natl. Acad. Sci. U. S. A.* **2018**, *115*, 9086−9091.

(18) Suzuki, Y.; Endo, M.; Sugiyama, H. *Nat. Commun.* **2015**, *6*, 8052.

(19) Yang, Y.; Wang, J.; Shigematsu, H.; Xu, W.; Shih, W. M.; Rothman, J. E.; Lin, C. *Nat. Chem.* **2016**, *8*, 476−483.

(20) Zhang, Z.; Yang, Y.; Pincet, F.; Llaguno, M. C.; Lin, C. *Nat. Chem.* **2017**, *9*, 653−659.

(21) Bian, X.; Zhang, Z.; Xiong, Q.; De Camilli, P.; Lin, C. *Nat. Chem. Biol.* **2019**, *15*, 830−837.

(22) Dong, Y.; Yang, Y. R.; Zhang, Y.; Wang, D.; Wei, X.; Banerjee, S.; Liu, Y.; Yang, Z.; Yan, H.; Liu, D. *Angew. Chem., Int. Ed.* **2017**, *56*, 1586−1589.

(23) Franquelim, H. G.; Khmelinskaia, A.; Sobczak, J.-P.; Dietz, H.; Schwille, P. *Nat. Commun.* **2018**, *9*, 811.

(24) Grome, M. W.; Zhang, Z.; Pincet, F.; Lin, C. X. *Angew. Chem., Int. Ed.* **2018**, *57*, 5330−5334.

(25) Shi, P.; Ju, E.; Yan, Z.; Gao, N.; Wang, J.; Hou, J.; Zhang, Y.; Ren, J.; Qu, X. *Nat. Commun.* **2016**, *7*, 13088.

(26) Xu, W.; Wang, J.; Rothman, J. E.; Pincet, F. *Angew. Chem., Int. Ed.* **2015**, *54*, 14388−14392.

(27) Chidchob, P.; Edwardson, T. G. W.; Serpell, C. J.; Sleiman, H. F. *J. Am. Chem. Soc.* **2016**, *138*, 4416−4425.

(28) Rizzuto, F. J.; Dore, M. D.; Rafique, M. G.; Luo, X.; Sleiman, H. F. *J. Am. Chem. Soc.* **2022**, *144*, 12272−12279.

(29) Dore, M. D.; Trinh, T.; Zorman, M.; de Rochambeau, D.; Platnich, C. M.; Xu, P.; Luo, X.; Remington, J. M.; Toader, V.; Cosa, G.; Li, J.; Sleiman, H. F. *Chem.* **2021**, *7*, 2395−2414.

(30) Albert, S. K.; Hu, X. L.; Park, S. J. *Small* **2019**, *15*, No. e1900504.

(31) Edwardson, T. G. W.; Carneiro, K. M. M.; McLaughlin, C. K.; Serpell, C. J.; Sleiman, H. F. *Nat. Chem.* **2013**, *5*, 868−875.

(32) Whitehouse, W. L.; Noble, J. E.; Ryadnov, M. G.; Howorka, S. *Bioconjugate Chem.* **2019**, *30*, 1836−1844.

(33) Zhao, Y.; Guo, L.; Cao, S.; Xie, M.; Peng, H.; Li, J.; Luo, S.; Ma, L.; Wang, L. *Chem. Commun.* **2023**, *59*, 306−309.

(34) Huo, S.; Li, H.; Boersma, A. J.; Herrmann, A. *Adv. Sci.* **2019**, *6*, 1900043.

(35) Rosler, A.; Vandermeulen, G. W.; Klok, H. A. *Adv. Drug Deliv Rev.* **2001**, *53*, 95−108.

(36) Wang, Y. Q.; Cheng, J.; Zhao, D.; Liu, Y.; Luo, T.; Zhong, Y. F.; Mo, F. L.; Kong, X. Y.; Song, J. *Nanoscale* **2020**, *12*, 23953−23958.

(37) Rahbani, J. F.; Vengut-Climent, E.; Chidchob, P.; Gidi, Y.; Trinh, T.; Cosa, G.; Sleiman, H. F. *Adv. Healthc. Mater.* **2018**, *7*, No. e1701049.

(38) Li, J.; Xun, K.; Pei, K.; Liu, X.; Peng, X.; Du, Y.; Qiu, L.; Tan, W. *J. Am. Chem. Soc.* **2019**, *141*, 18013−18020.

(39) Trinh, T.; Chidchob, P.; Bazzi, H. S.; Sleiman, H. F. *Chem. Commun.* **2016**, *52*, 10914−10917.

(40) Kang, Y.; Liu, J.; Jiang, Y.; Yin, S.; Huang, Z.; Zhang, Y.; Wu, J.; Chen, L.; Shao, L. *Adv. Drug Delivery Rev.* **2021**, *175*, 113820.

(41) Dougherty, P. G.; Sahni, A.; Pei, D. *Chem. Rev.* **2019**, *119*, 10241−10287.